Crystal structures of molybdenum borides dictate electrocatalytic ammonia synthesis efficiency

Guiming Peng [a,b,*,1], Jian-Wen Zhao [c,1], Jiaqi Wang [b], Eli Hoenig [b], Suqin Wu [a], Mingzhan Wang [b], Mao He [a], Lei Zhang [a], Jin-Xun Liu [c,**], Chong Liu [b,**]

[a] *College of Chemistry and Chemical Engineering, National Engineering Research Center for Carbonhydrate Synthesis, Key Lab of Fluorine and Silicon for Energy Materials and Chemistry of Ministry of Education, Jiangxi Normal University, Nanchang, Jiangxi 330022, China*
[b] *Pritzker School of Molecular Engineering, University of Chicago, Chicago, IL 60637, United States*
[c] *Department of Chemical Physics, University of Science and Technology of China, Hefei 230026, China*

ARTICLE INFO

ABSTRACT

Rather than multivalence molybdenum (Mo), the low valence Mo has rarely been reported as active site for nitrogen reduction. Herein, molybdenum borides with various Mo-B stoichiometry ratios (Mo_2B, α-MoB, and Mo_2B_4) in which Mo shows low valence (<1) are synthesized as electrochemical nitrogen reduction reaction (eNRR) catalysts. Mo_2B_4 demonstrates the highest NH_3 yield of 7.65 μg h^{-1}/mg at − 0.15 V with Faradaic efficiency (FE) of 12.47 %, while α-MoB exhibits the fastest intrinsic eNRR reaction rate with a higher FE of 17.17 % after considering electrochemically active surface area. DFT calculations reveal that both enzymatic and consecutive mechanisms via side-on configuration can proceed on α-MoB. Additionally, α-MoB exhibits suppressed HER activity due to an optimal surface B occupancy. The eNRR of molybdenum borides were verified qualitatively and quantitatively by $^{15}N_2$ isotope experiments. This study demonstrated a synergistic design of eNRR and HER activity to achieve efficient electrocatalytic ammonia production with high eNRR selectivity.

1. Introduction

Electrocatalytic synthesis of value-added chemicals, such as NH_3 [1, 2], H_2O_2 [3], organic synthesis [4,5], represents an emerging way for decarbonization [6]. In recent years, electrocatalytic nitrogen reduction reaction (eNRR) has received tremendous interest [7–9]. The eNRR technology can be compatible with smaller-scale and distributed production facilities with less energy consumption and lower CO_2 emission. Nevertheless, the low polarity and extremely strong N≡N triple bond led to difficult protonation of N_2 molecule. Additionally, the equilibrium potential of eNRR is close to that of hydrogen evolution reaction (HER) [10], which causes low selectivity of eNRR due to the strong competition from HER. The design and synthesis of efficient eNRR catalysts with high selectivity and high NH_3 yield is still a great challenge and far from industrial-scale implementation [8].

To date, transition metals (TMs)/compounds have been most intensively investigated as eNRR catalysts due to their occupied and empty *d*-orbitals.[11–18] The empty *d*-orbitals of TMs would accept electrons from the lone-pair electrons of dinitrogen molecule. Meanwhile, the electrons in the occupied *d*-orbitals could be backdonated to the adsorbed N_2 molecule thus activating the N≡N bond.[14,19] Mo is one of the two metal elements (Mo and Fe) in natural nitrogenase and has strong affinity to dinitrogen molecule [20]. Mo clusters and their complexes have been experimentally and theoretically reported to show promising activity in electrocatalytic ammonia synthesis [12,21–27]. For instance, in 2003 Yandulov and Schrock reported the first catalytic transformation of dinitrogen into ammonia under ambient condition using Mo-triamidoamine as a catalyst [28]. Density functional theory (DFT) calculations showed that Mo atoms supported on boron nitride is able to activate N_2 and stabilize N_2H but destabilize NH_2 [12]. Single Mo atoms on N-doped carbon [29] and carbon nitride [30] were demonstrated to show low overpotential for eNRR. Mo complexes such as MoS_2 [24,31,32], Mo_2C [33], MoO_x,[34] Mo-based alloy clusters [35,36], have been proved as efficient catalysts towards eNRR. All these reports

indicate that Mo in materials are active sites in adsorbing and activating N_2.

It is noted that Mo element in the above-indicated materials is multivalent. Whether low-valent molybdenum is active for eNRR remains an open question. Molybdenum borides with low-valent (<1) molybdenum have not been systematically investigated as eNRR catalyst by experimentation, though several computational studies demonstrate that molybdenum borides are promising in eNRR application [37,38], and MoB was mentioned in a Mo-Al-B ternary eNRR catalyst.[39] Molybdenum borides are a family of materials showing excellent electric conductivity, good solvent-resistant stability, and tunable composition [40,41]. Fokwa et al. have revealed that molybdenum borides exhibit boron-dependent HER activity [40]. This property could be utilized to modulate the eNRR selectivity, since HER is the major competing reaction. Given that molybdenum borides come with different stoichiometries and crystal structures, the influence of material characteristics on eNNR remains largely unknown, therefore, it is important to identify the structure-activity relationship and the optimal eNRR catalysts in the molybdenum borides family.

In this study, molybdenum borides with different chemical compositions (Mo_2B, α-MoB, and Mo_2B_4) were synthesized as eNRR catalysts. The atomic surface occupancy of Mo to B can be tuned correspondingly by changing the stoichiometry of molybdenum boride compounds. The eNRR investigation showed that these molybdenum borides demonstrated the maximum NH_3 yields at -0.15 V vs RHE with yields of 0.99 μg h^{-1} mg^{-1}, 5.45 μg h^{-1} mg^{-1}, 7.65 μg h^{-1} mg^{-1} and Faradaic efficiencies (FE) of 3.35 %, 17.17 %, and 12.47 % for Mo_2B, α-MoB, and Mo_2B_4, respectively. Quantitative $^{15}N_2$ isotope experiments confirmed the nitrogen reduction and NH_3 yield. Considering the different electrochemical surface areas, the normalized eNRR performance showed that α-MoB has the fastest eNRR reaction rate, which is a result of the optimal Mo to B atomic surface occupancy. DFT calculation reveals that, with intermediate B content in α-MoB, the reaction intermediates bind not too weakly or too strongly which is opposite to the case of Mo_2B and Mo_2B_4, giving α-MoB the highest activity of eNRR.

2. Experimental section

2.1. Synthesis of molybdenum borides

The molybdenum borides (Mo_2B, α-MoB, and Mo_2B_4) were synthesized as following. Firstly, the precursors molybdenum metal power and boron powder were mixed at different stoichiometric ratios (2:1, 1:1, 1:2) targeting at different final molybdenum borides. These precursor mixture powders were pelletized and followed with thermal transformation at 1100 °C for 4 h in Ar atmosphere. Molybdenum borides were obtained after the system is cooled down. The material characterizations could be found in Supplementary Material.

2.2. Electrochemical measurements

The nitrogen reduction reaction (NRR) experiments were carried out using a three-electrode Nafion membrane-separated H-cell on a BioLogic VMP3 potentiostat system. Before device assembling, the Nafion membrane was pretreated in 5 % H_2O_2 aqueous solution at 80 °C for 1 h and in ultrapure water at 80 °C for 1 h successively. Ag/AgCl (saturated KCl) electrode and Pt foil are used as the reference electrode and counter electrode, respectively. 0.1 M HCl aqueous solution is used as electrolyte in this study. To avoid the possible NH_3 and trace NO_x contamination from feeding N_2 gas (99.999 %), it was bubbled through a H_2SO_4 (2 M) aqueous solution and 1 M KOH aqueous solution before fed into the electrolyte. The electrolyte is saturated with N_2 for 30 min ahead of NRR experiments. During NRR experiment, a constant N_2 flow was fed into the electrolyte at the cathode half-cell. For data analysis, all potentials were converted into values versus reversible hydrogen electrode (RHE) by the Nernst equation. $^{15}N_2$ isotopic experiment was performed using

the same setup while coupling with a gas collector to cycle the $^{15}N_2$ gas. For successive NRR performance stability test, the electrolyte (0.1 M HCl) was refreshed for each cycle (four hours) but using the same molybdenum boride electrode.

To obtain double-layer capacitance (C), cyclic voltammetry (CV) measurements at different scan rates in non-Faradaic range of 0.1–0.2 V vs RHE were performed. As the relationship between the charging current (i_c) and scan rates (v) and C is $i_c = vC$. C can be obtained from the slope of i_c–v plot.

2.3. Indophenol blue method for determination of ammonia concentration

The concentration of ammonia in electrolyte was determined using the indophenol blue method. 1 Specifically, 1 mL of the electrolyte was added into 1 mL solution which was composed of 1 M NaOH and 5 wt% salicylic acid and 5 wt% sodium citrate. Then 0.5 mL of 0.05 M NaClO aqueous solution was added, followed by addition of 0.1 mL of sodium nitroferricyanide (1 wt%) aqueous solution. After settling for 1 h, the UV–vis spectra was collected. The NH_3 production was indicated by the formation of indophenol blue, which was determined by the absorbance at 655 nm, with its concentration calibrated by a standard plot using a serial of concentration-known ammonium chloride solutions.

2.4. ^1H NMR determination of $^{15}NH_3$

^1H NMR tests were performed on a Bruker Avance 400-MHz system. ^1H NMR samples were prepared by mixing the electrolyte with DMSO-d$_6$ at 9/1 ratio. $^{15}NH_4Cl$ standard solutions with set concentrations (0.1 μg/mL, 0.2 μg/mL, 0.4 μg/mL, 0.6 μg/mL) were prepared using DI water-DMSO-d6 (9/1) as solvent. For all these samples, maleic acid ($C_4H_4O_4$) was added as the internal standard with its concentration of 1 mM.

2.5. Determination of hydrazine production

Firstly, a color reagent was prepared by mixing 3 g of para-(dimethylamino) benzaldehyde and 15 mL of 12 M HCl aqueous solution into 150 mL of absolute ethanol. Then 1 mL of the above solution was mixed with 1 mL of the electrolyte in our study. After settling for 10 min, the mixture was detected by the UV–vis spectroscopy at the wavelength of 455 nm.

2.6. DFT calculations

DFT calculations were performed to study NRR mechanism on the most favorable surfaces of α-MoB, Mo_2B and Mo_2B_4 phases by using the Vienna ab initio simulation package (VASP). The details of DFT calculations were illustrated in Supplementary Material.

3. Results and discussion

3.1. Material characterizations and analysis

The synthesis of molybdenum borides was illustrated in Fig. 1a. Briefly, molybdenum powder was mixed with boron powder at different stoichiometric molar ratios (2:1, 1:1, and 1:2 for Mo_2B, α-MoB, and Mo_2B_4, respectively) first. The mixed powder was pelletized, and subsequently it underwent the thermal transformation at 1100 °C in Ar atmosphere for 4 h. SEM images showed that molybdenum boride particles of different compositions largely inherited the size of molybdenum metal particles but lost the morphological features of Mo particles and B powders (Figs. 1b-d, S1). The high temperature thermal synthesis led to surface roughness increase. Cracks appeared on Mo_2B_4 particles (Fig. 1d). X-ray diffraction (XRD) patterns showed that the characteristic peaks of Mo and B powder (Fig. S2a) disappeared after thermal transformation (Fig. 1e). The XRD patterns are indexed well with Mo_2B (PDF
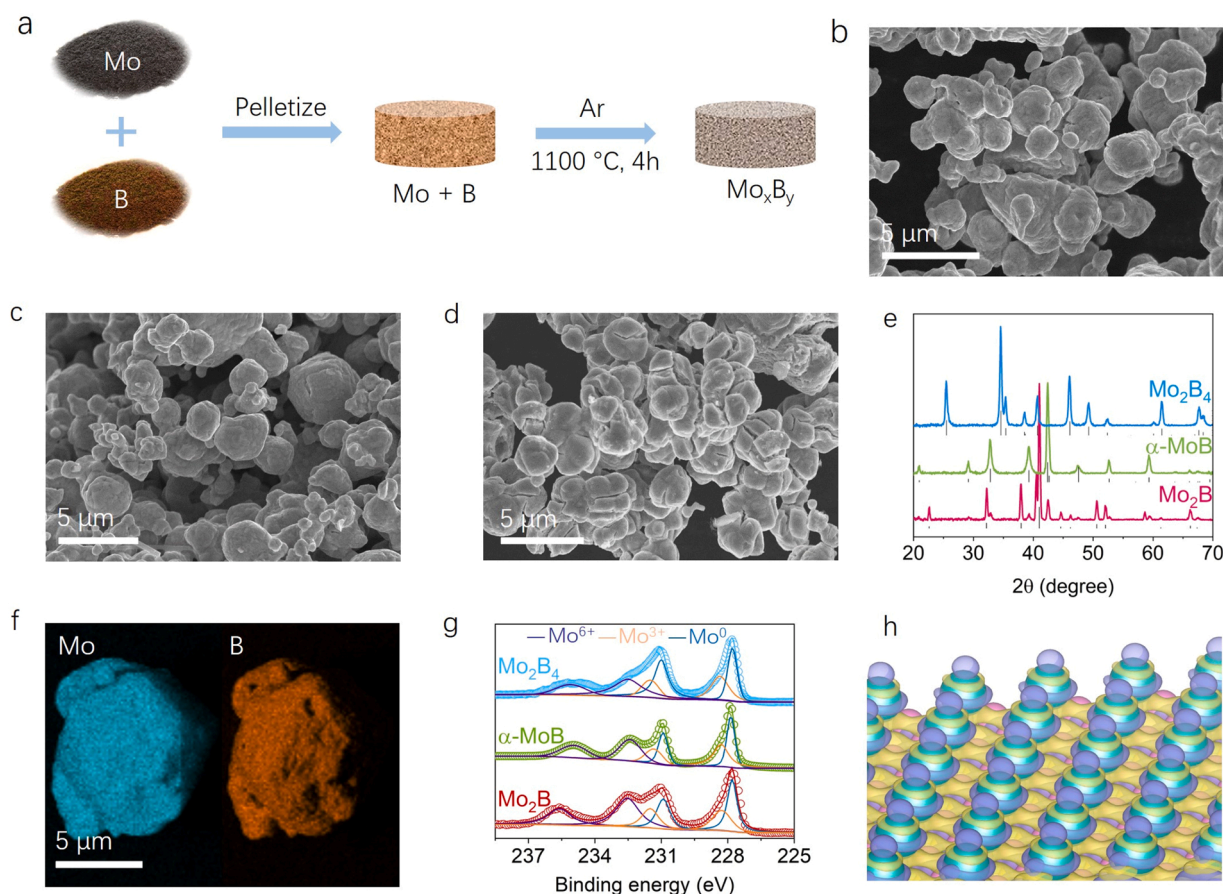
Fig. 1. (a) Schematic illustration of the synthesis of molybdenum borides. (b-d) SEM images of (b) Mo_2B, (c) α-MoB, (d) Mo_2B_4. (e) XRD patterns of Mo_2B, α-MoB and Mo_2B_4. (f) EDS elemental mapping of Mo_2B_4. (g) Mo_{3d} XPS spectra of Mo_2B, α-MoB, and Mo_2B_4 powder. (h) The electron density difference of Mo_2B_4. Mo and B atoms were represented by cyan and pink balls, respectively. The yellow and purple iso-surfaces indicate the gain and loss of electron density, respectively.

No. 25-0561), α-MoB (PDF No. 41-0940), and Mo_2B_4 (PDF No. 01-077-0807), respectively (Fig. 1e), demonstrating the successful synthesis of molybdenum borides. Further tuning the molar ratio of B/Mo from 2:1–3:1 or to even higher ratio before thermal transformation cannot shift the final composition of molybdenum boride using the method in this study (Fig. S2b). High resolution transmission electron microscopy (TEM) images further confirm the successful synthesis of molybdenum boride materials (Fig. S3). Energy dispersive spectroscopy (EDS) images proved the uniform distribution of Mo and B over the same particle for all Mo_2B, α-MoB, and Mo_2B_4 materials (Figs. 1f and S4). It is worthwhile to mention that the used approach for synthesizing molybdenum boride in the present study is less harsh than the reported methods in literature such as arc-melting synthesis using current up to 60 A [40], chemical vapor deposition using high-purity H_2 gas as carrier gas [42], and the solid state reaction requiring high pressure and high vacuum condition [43,44]. As the molybdenum borides in this study are derived from boronization of Mo particles, precise control of the morphology of molybdenum borides particles with well-defined facet exposure still remains a challenge like other reported synthesis methods [45]. Despite of this, the obtained molybdenum borides showed different crystal structures. It is of great significance to investigate the material phase related characteristics in NRR electrocatalysis.

The surface chemistry of as-synthesized Mo_2B, α-MoB, and Mo_2B_4 were characterized by X-ray photoelectron spectroscopy (XPS). The Mo_{3d} and B_{1s} XPS are presented in Fig. 1g and S5. Mo^0 peaks at 227.8 eV and 230.9 eV (Fig. 1g) and B^0 peaks at 187.7 eV and 188.5 eV (Fig. S5) attributed to molybdenum borides are observed for all three materials. The appearance of Mo^{3+} peaks at 228.26 eV and 231.48 eV, and Mo^{6+} peaks at 232.51 eV and 235.56 eV indicate the surfaces of molybdenum

borides are partially oxidized, which have been revealed by others [40, 46,47]. For B1s XPS spectra, besides B^0 peaks of molybdenum borides, the peaks at 192.06 eV and 192.92 eV are attributed to B_2O_3 while the peak at 189.8 eV belong to H_2BO_3 [40]. The surface oxidation of Mo_2B, α-MoB, and Mo_2B_4 varied from each other. α-MoB is most vulnerably being oxidized upon exposure to air, evidenced by the most oxidized states and minimum Mo^0 and B^0 states in XPS spectra (Figs. 1g, S5) [40]. Despite of this, the oxide signals in XRD pattern cannot be discerned (Fig. 1e), indicating the low presence of oxide species. XPS spectra of the sample after Ar ion etching confirm the surface oxidation occurs only at the surface while its inner composition remains as molybdenum borides (Fig. S6). TEM-EDS element mapping results also show minimal oxygen content and the O element distributed mainly on the surface (Fig. S7). The molybdenum oxides can be electrochemically reduced by linear scanning voltammogram (LSV) processing in the potential range from − 0.2 V to 0 V vs RHE. The reduction peak of molybdenum oxides at ∼ − 0.1 V vs RHE is greatly reduced after the first LSV scan and is completely vanished after several LSV scans (Fig. S8) [46]. Note that the surface boron oxides can be readily dissolved into electrolyte with no influence on the later electrocatalytic application. The low valence state of Mo in molybdenum borides was further confirmed by Bader charge analysis via DFT calculations. The charge state of Mo and B in Mo_2B_4, Mo_2B, and α-MoB are + 0.68 and − 0.34, + 0.45 and − 0.71, and + 0.59 and − 0.59, respectively (Figs. 1h and Fig. S9).

The electrochemically active surface area (ECSA) was tested to evaluate the potential of the as-synthesized molybdenum borides in electrocatalytic ammonia production. Fig. 2a shows the current at 0.15 V vs RHE as a function of scan rate during cyclic voltammogram (CV) measurements. The derived ECSA ratios relative to Mo powder
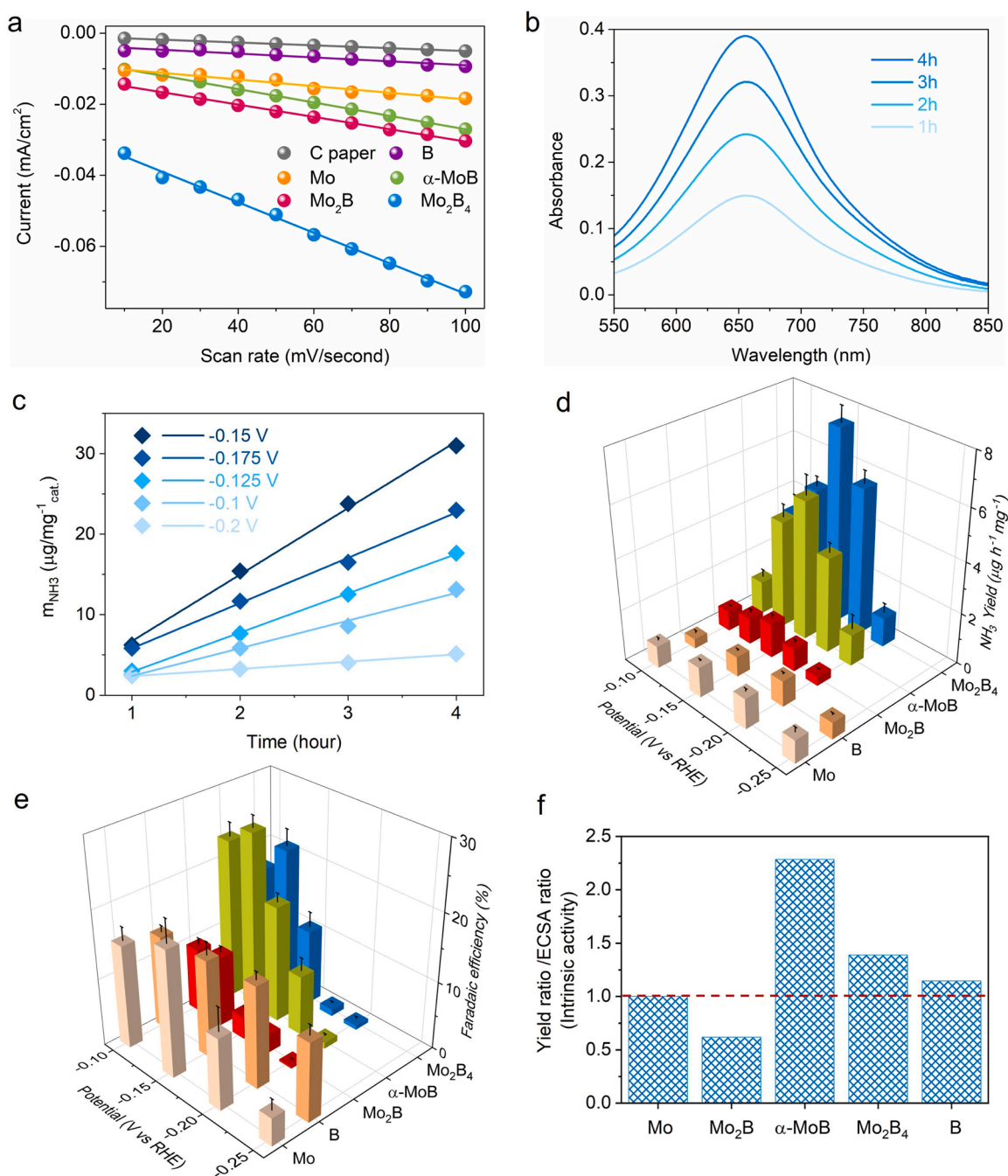
Fig. 2. (a) The cathodic charging currents of C paper, Mo, B, Mo$_2$B, α-MoB, Mo$_2$B$_4$ at 0.15 V vs RHE as a function of scan rates. (b) UV–vis spectra of the electrolyte stained with indophenol indicator at different time durations at the potential of − 0.15 V versus RHE by using Mo$_2$B$_4$ as a catalyst. (c) Ammonia concentration in electrolyte as a function of time at − 0.1, − 0125, − 0.15, − 0.175 and − 0.2 V vs RHE, respectively, when using Mo$_2$B$_4$ as a catalyst in N$_2$. (d) Ammonia production yields, and (e) Faradaic efficiencies of Mo$_2$B, α-MoB, Mo$_2$B$_4$, Mo, and B at different potentials in N$_2$ saturated 0.1 M HCl aqueous solution. (f) The intrinsic activity of Mo, Mo$_2$B, α-MoB, Mo$_2$B$_4$ and B in term of Yield ratio/ ECSA ratio (with respect to Mo).

were shown in Fig. S9. Clearly, the loading of molybdenum borides, boron and Mo on carbon paper showed higher ECSA values than bare C paper electrode (Figs. 2a, S10), meaning the introduced electrochemically active sites. Molybdenum borides demonstrated higher ECSA than Mo powder and B powder. Mo$_2$B$_4$ showed highest ECSA while Mo$_2$B displayed the lowest among the three molybdenum borides (Figs. 2a, S10).

3.2. NRR experimental study

The eNNR was performed in a Nafion membrane separated H-cell. To

eliminate the possible ammonia and trace NO$_x$ contamination in nitrogen gas, the nitrogen gas was bubbled through a 2 M H$_2$SO$_4$ aqueous solution and 1 M KOH aqueous solution before fed into the cathode half-cell. LSV curves showed the three as-synthesized molybdenum borides exhibited a B-dependency HER activity with Mo$_2$B$_4$ showed the highest HER performance (Fig. S11). When feed N$_2$ in, the current increase was observed in LSV curve comparing to that under argon, which should be contributed to the nitrogen reduction reaction (Fig. S12). The ammonia production accumulated in the electrolyte was monitored by the indophenol method manifested as an increase in UV–vis absorbance. Its concentration was calibrated by a standard plot which shows excellent

concentration-absorbance correlation (Fig. S13). UV–vis spectra of the electrolytes at different reaction stages stained with indophenol indicator showed increased absorbance over reaction time (Fig. 2b). This means the ammonia is electrocatalytically produced. The ammonia content in electrolyte increases linearly over reaction time (Fig. 2c). Like our previous report [48], the ammonia production yield is obtained from the slope of m_{NH3}-time plots, which rules out the possible false NH_3 contribution from background. It is found that all Mo_2B, $α$-MoB, and Mo_2B_4 demonstrated a peak NH_3 yield at -0.15 V vs RHE with the values of 0.99 $μg\ h^{-1}\ mg^{-1}$, 5.45 $μg\ h^{-1}\ mg^{-1}$, 7.65 $μg\ h^{-1}\ mg^{-1}$, respectively (Fig. 2d). FEs of Mo_2B_4 at -0.1 V, -0.125 V, -0.15 V and -0.175 V vs RHE are 17.14 %, 21.49 %, 12.5 %, and 1.02 % (Fig. 2e), respectively. The FE decreased at more negative potential because of the increasingly pronounced competing HER. At the peak yield potential

$(-0.15$ V), $α$-MoB showed the highest FE (17.17 %) among the three molybdenum borides. The peak yield and peak FE are identified at different potentials for different materials, which is because the FE is determined by the rate competition between eNRR and HER, so that higher HER activity (such as Mo_2B_4) deteriorates the FE. The peak FEs of Mo_2B and $α$-MoB are at -0.125 V vs RHE (same as Mo_2B_4) with the values of 10.33 % and 26.05 % (Fig. 2e).

Control experiments performed under open circuit condition (Fig. S14) and Ar atmosphere at -0.15 V (Fig. S15) show no ammonia increase in the electrolyte. No hydrazine production was observed during the eNRR process (Fig. S16), indicating the good selectivity of eNRR by using the molybdenum borides as catalysts. All the above evidence confirms the successful electrocatalytic ammonia production at the surface of molybdenum boride. Mo and B powder were further used
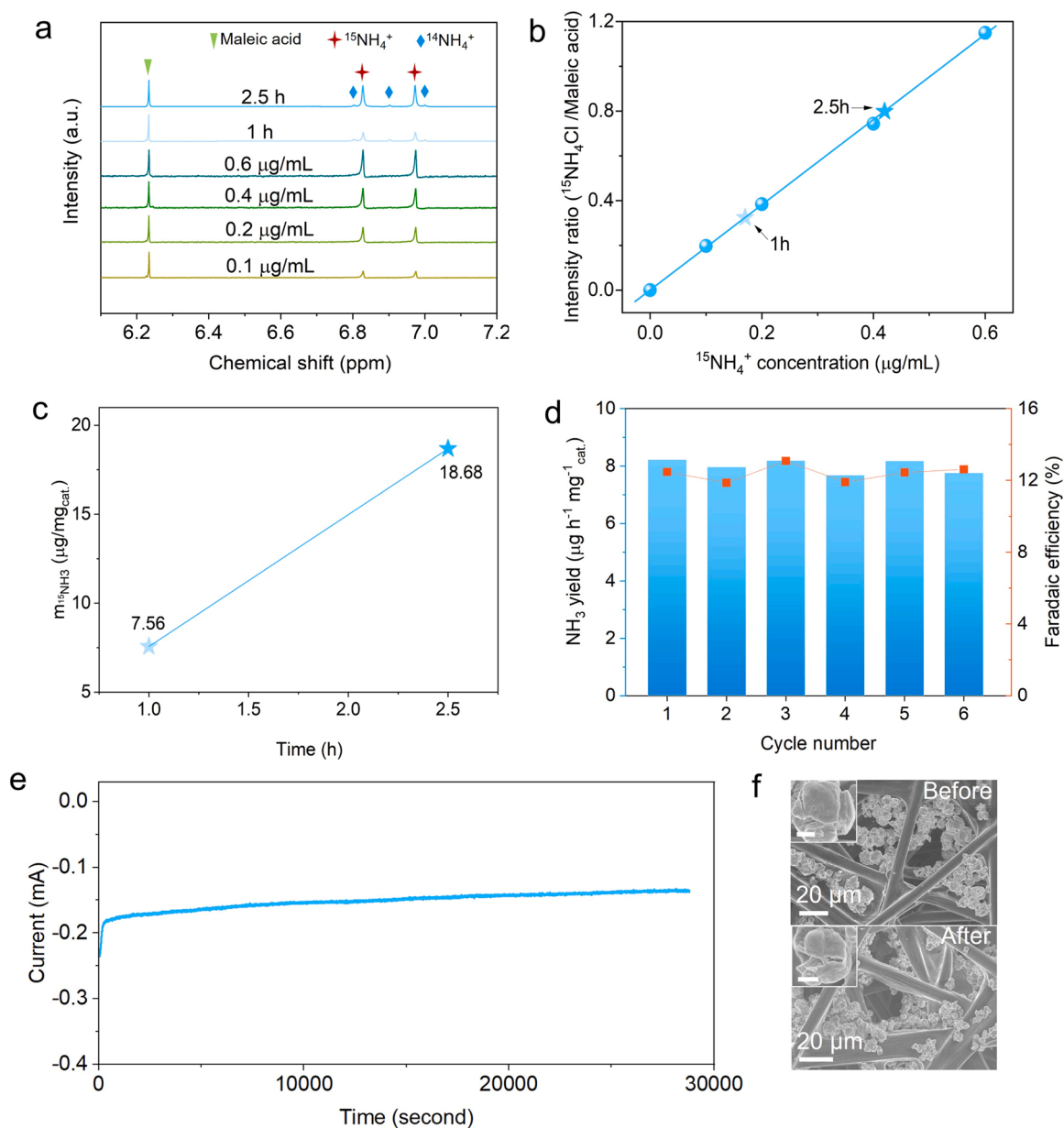

Fig. 3. (a) ^{1}H NMR of $^{15}NH_4Cl$ aqueous solutions of different concentrations and the electrolyte at different reaction durations (1 h and 2.5 h) when feeding $^{15}N_2$ at -0.15 V vs RHE using Mo_2B_4 as catalyst. Maleic acid was used as an internal standard; (b) the linear plot of ^{1}H NMR intensity ratio ($^{15}NH_4Cl$/Maleic acid)-$^{15}NH_4^+$ concentration. The ^{1}H NMR intensity ratios of the electrolyte after reaction for 1 h and 2.5 h under $^{15}N_2$ atmosphere are indicated by the arrows; (c) the $^{15}NH_3$ produced at different reaction durations. (d) Ammonia production stability and Faradaic efficiency stability of Mo_2B_4 over 6 successive eNRR measurements at -0.15 V vs RHE in N_2 saturated 0.1 M HCl aqueous solution. (e) Current stability of Mo_2B_4 at -0.15 V vs RHE. (f) SEM image of Mo_2B_4 on C paper before and after current stability test. Insets in (f) are the individual Mo_2B_4 particles before and after stability test with the scale bar of 2 μm.

as catalysts for comparison. Mo powder exhibited a peak yield of 1.18 µg h^{-1} mg^{-1} at − 0.15 V vs RHE with FE of 18.6 % (Figs. 2d and 2e), while that of B powder is 1.01 µg h^{-1} mg^{-1} at − 0.2 V vs RHE with FE of 14.97 % (Figs. 2d and 2e). The peak NH$_3$ yield of Mo$_2$B$_4$ is over seven-times higher than that of Mo and B powders. The moderate FEs of Mo and B are mainly ascribed to the low HER activity (Fig. S11). These findings indicate the synergistic effect of Mo and B sites at the surface of Mo$_2$B$_4$.

Considering the different ECSA of the three molybdenum boride electrodes, the yield (at −0.15 V) ratio (with respect to Mo) normalized by ECSA ratio (with respect to Mo) was used as a descriptor to evaluate the intrinsic eNRR activity of the catalysts (Fig. 2 f). The Yield ratio/ ECSA ratio values of α-MoB and Mo$_2$B$_4$ are higher than Mo and B while that of Mo$_2$B is lower. Different from the yield, α-MoB showed the highest Yield ratio/ECSA ratio (Fig. 2 f), meaning its highest intrinsic eNRR activity.

^{15}N$_2$ isotope experiment further proved the production of NH$_3$ from nitrogen reduction at the catalyst surface. As Mo$_2$B$_4$ showed the highest NH$_3$ yield at − 0.15 V vs RHE, though not the best intrinsic activity, it was selected to perform ^{15}N$_2$ isotope experiment. Fig. 3a shows the ^{1}H NMR results when using Mo$_2$B$_4$ as electrocatalyst. Obviously, ^{15}NH$_4^+$ signal at 6.83 and 6.97 ppm was detected (Fig. 3a). To quantitively analyze the NH$_3$ yield, maleic acid was used as the internal standard

during ^{1}H NMR test. For standard ^{15}NH$_4^+$ solutions, ^{15}NH$_4^+$ signal intensity shows good correlation to its concentration (Fig. 3a–b). During eNRR experiment, the intensity of ^{15}NH$_4^+$ signal increased over time, suggesting NH$_3$ is produced from eNRR (Fig. 3a). At − 0.15 V when using Mo$_2$B$_4$ as catalyst, the ^{15}NH$_3$ yield is 7.41 µg^{-1} h^{-1} mg^{-1} (Fig. 3c), slightly lower but in good accordance with that under normal N$_2$ atmosphere (7.65 µg h^{-1} mg^{-1}). Tiny ^{14}NH$_4^+$ signal was observed due to the trace ^{14}NH$_4$Cl impurity in HCl electrolyte. All these evidences confirmed the NH$_3$ production from nitrogen reduction. The molybdenum boride showed excellent stability in eNRR performance and chemical structure. As is shown in Fig. 3d, no decay in NH$_3$ yield and FE for Mo$_2$B$_4$ were seen over six successive cycles of performance measurements. In addition, the continuous reduction current at − 0.15 V vs RHE for 8 h showed merely 13.2 % decrease (Fig. 3e). SEM images showed the Mo$_2$B$_4$ particles are stable during eNRR test with no change in morphology (Fig. 3 f). XPS measurement revealed good chemical stability of Mo$_2$B$_4$ during eNRR experiment with no obvious differences between XPS spectra of before and after eNRR test (Fig. S17).

3.3. NRR mechanism study

To shed light on the crystal phases sensitivity of molybdenum borides, we resort to DFT calculations [49,50] for studying the mechanism
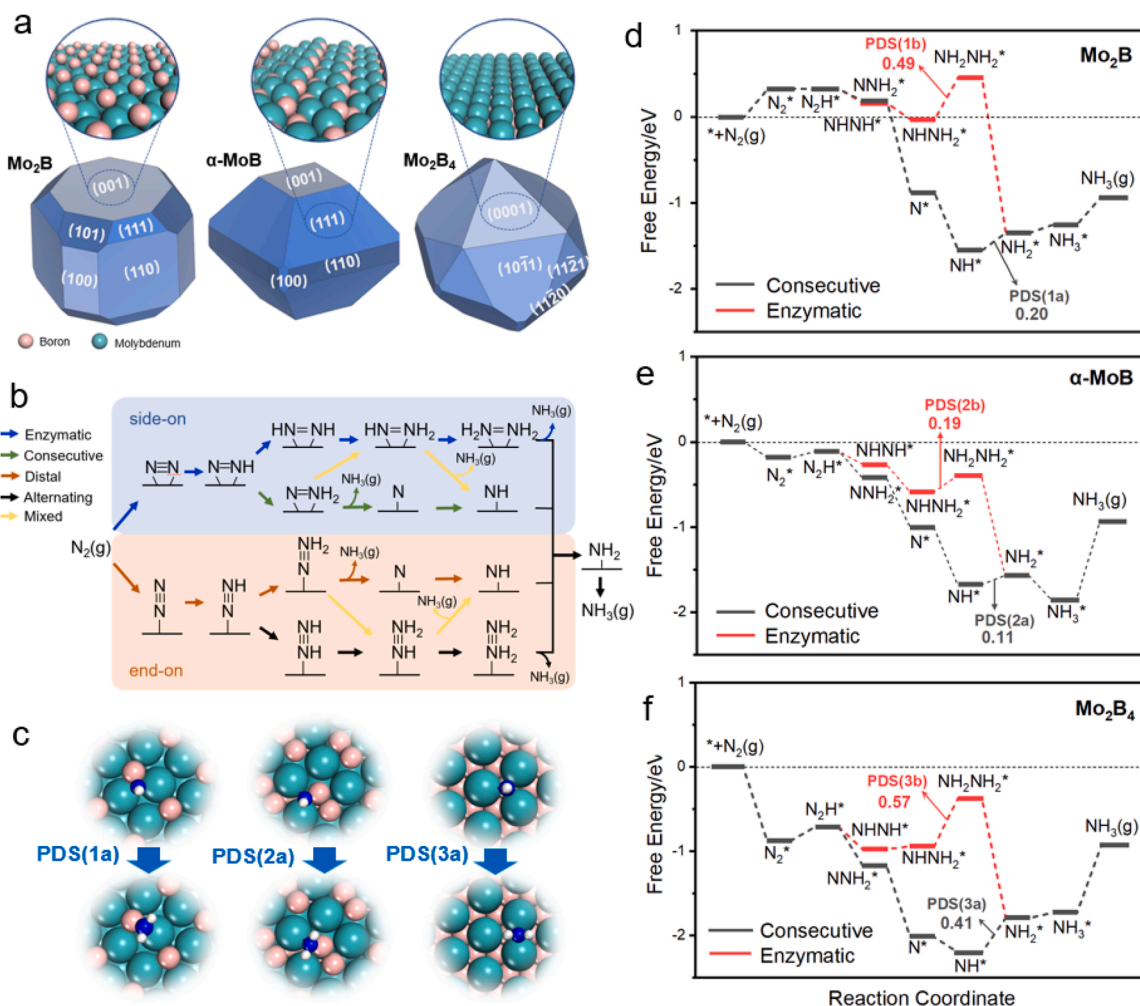

Fig. 4. DFT calculation study on the mechanism of eNRR over different phases of molybdenum borides. (a) Wulff shapes of Mo$_2$B α-MoB, Mo$_2$B$_4$ determined by DFT calculations and corresponding most energetically stable surface structures. (b) Scheme for the possible reaction mechanism of eNNR. (c) Configuration of the adsorbed species for the potential-determining step in the optimal reaction path. (d – f) Potential Gibbs free energy of eNRR following Enzymatic and Consecutive mechanism. PDS(1a), PDS(2a), PDS(3a) indicates the potential determination step of Consecutive mechanism, and PDS(1b), PDS(2b), PDS(3b) represents the potential determination step of Enzymatic mechanism. The limiting potential is given in V unit.

of eNRR over the most favorable exposed surfaces of Mo_2B, α-MoB and Mo_2B_4. First, we calculated the surface energies and found the (001) of Mo_2B, (111) of α-MoB, and (0001) of Mo_2B_4 facets have the lowest surface energies ranging from 153 meV/$\mathring{A}^2$ to 160 meV/$\mathring{A}^2$ (Tables S1–S3). Meanwhile, they have the largest contributions (Fig. 4a) to the overall surface area of the Wulff shapes of Mo_2B, α-MoB and Mo_2B_4, respectively. Generally, the concentration of Mo atoms at the surface increases by decreasing the atomic ratio of Mo/B in molybdenum borides (Fig. S18). $Mo_2B(001)$ and $Mo_2B_4(0001)$ surfaces are terminated purely by B and Mo atoms, respectively, whereas the surface of α-MoB(111) contains both Mo and B atoms (Fig. S18). N_2 molecules prefer to be chemically adsorbed at the Mo site to B site.

Five different electrochemical NRR mechanisms (Fig. 4b), namely Enzymatic, Consecutive, Distal, Alternating and Mixed mechanisms [51], were extensively studied over the most stable $Mo_2B(001)$, α-MoB (111) and $Mo_2B_4(0001)$ surfaces to reveal the crystallographic dependence of eNRR on molybdenum borides. Among them, enzymatic and consecutive mechanisms appear side-on intermediates adsorption patterns, whereas distal and alternating mechanisms show end-on intermediates adsorption patterns. For consecutive and distal mechanism, the adsorbed N_2 is hydrogenated by two protons in the formation of $NNH_2 *$, followed by the formation and desorption of ammonia. Regarding to the enzymatic and alternating mechanism, two N atoms in adsorbed N_2 molecule can be hydrogenated alternatively, generating the key $NHNH *$ and $NH_2NH_2 *$ intermediates for ammonia synthesis. Whereas for the mixed mechanism, eNRR proceeds via alternating mechanism after one or two hydrogenation steps following distal

mechanism (Fig. 4b, Tables S4–S6). The Gibbs free energy diagrams for eNRR at 0 V vs RHE following the consecutive and enzymatic mechanisms are given in Figs. 4d–4 f with others presented in Figs. S19–S21.

Generally, the hydrogenation of $NHNH_2 *$ and $NH *$ towards NH_2NH_2 $*$ and $NH_2 *$ are the potential determination step (PDS) for the consecutive and enzymatic mechanisms over the three molybdenum boride phases, respectively (Figs. 4d–4 f and Fig. S19–S24). Results show that all three molybdenum borides prefer side-on eNRR reaction configuration. Both enzymatic and consecutive mechanisms can proceed together over α-MoB(111) surface with the limiting potential (U_L) difference of 0.08 V (Fig. 4e). However, over $Mo_2B(001)$ and $Mo_2B_4(0001)$ surfaces, the eNRR prefers the consecutive mechanism with the U_L lower by -0.29 V and -0.16 V, respectively. In addition, for the three molybdenum borides, the mixed II mechanism in side-on configuration has the same favorable U_L as that of consecutive mechanism (Figs. S19–S21). Moreover, the Gibbs free energy diagrams of Enzymatic and Consecutive mechanisms for eNRR on the most stable Mo (110) surface and the most stable B (10$\bar{1}$) surface show Mo ($U_L = -0.39$ V, Fig. S25) and B ($U_L = -0.81$ V, Fig. S26) have higher U_L than α-MoB ($U_L = -0.11$ V), indicating a lower eNRR activity than α-MoB. Our DFT calculations clearly revealed that α-MoB has the lowest U_L and thus highest intrinsic eNRR activity towards ammonia (Figs. 4d–4 f).

The eNRR activity of molybdenum borides is influenced by the adsorption strength of intermediates on catalyst surface. Electronic structure analysis, namely density of states (DOS), Bader charge, electronic charge density difference and crystal orbital Hamilton population (COHP) analysis for the key NH intermediate adsorption were
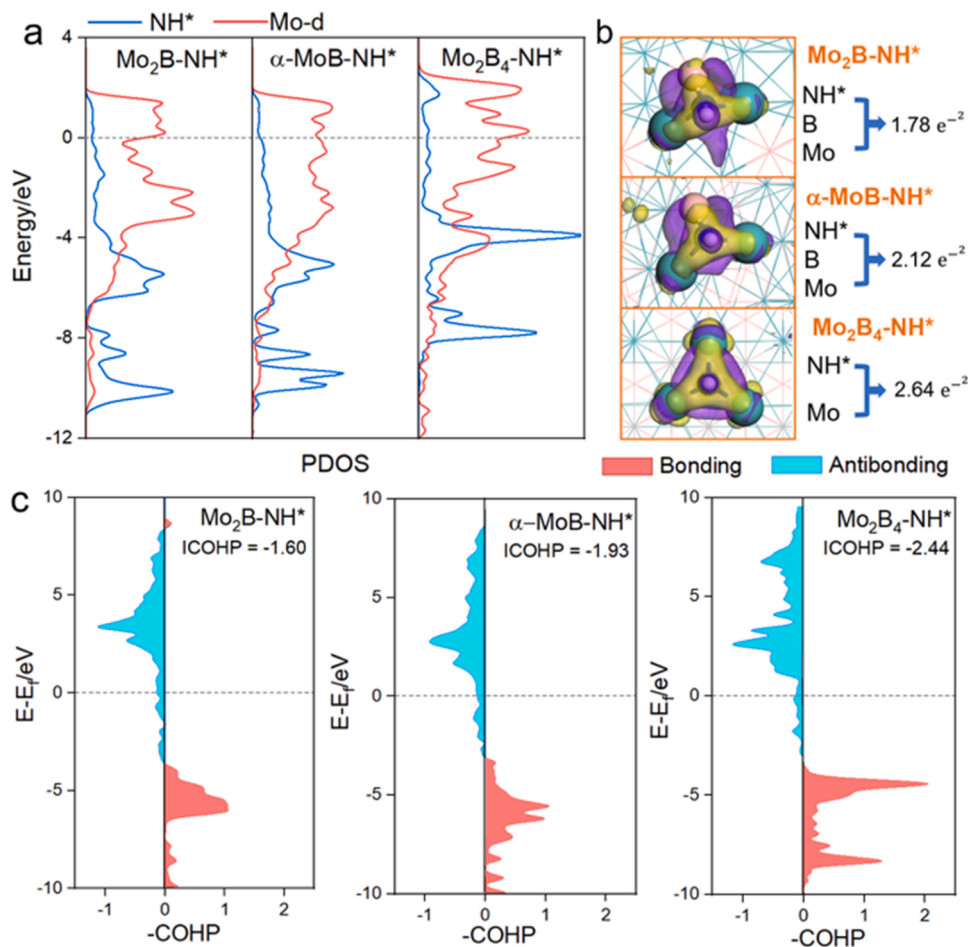

Fig. 5. (a) Projected density of states, (b) electronic charge density difference and the electrostatic interactions analysis between the two charges and (c) crystal orbital Hamilton population analysis of NH adsorption on Mo_2B, α-MoB and Mo_2B_4 surfaces. The product of the two charges between Mo and NH fragments are given e⁻. The yellow and purple iso-surfaces indicate the gain and loss of electron density in the charge density difference analysis for NH adsorption.

performed to illustrate the different catalytic performance of eNRR over the three different molybdenum borides catalysts (Fig. 5). The stronger hybridization between NH and surface Mo leads to a stronger NH adsorption on molybdenum borides. Clearly, the Bader charge and COHP analysis demonstrate stronger adsorption of NH when decreasing Mo/B ratio in molybdenum borides (Figs. 5, S27), which increases the electrostatic interactions and thus decreases the antibonding interaction between NH and Mo fragments. An optimal catalyst has to bind to the reactants at an intermediate strength which is neither too weak nor too strong [52]. Due to the electronegativity of B atom in molybdenum borides while Mo sites are slightly positively charged as revealed by the electronic charge density difference diagram (Figs. 1h and S9), the key NH*, N_2H* and NNH_2 * intermediates adsorb much weaker on the B-terminated $Mo_2B(001)$ surface with Gibbs free energy higher than 0 eV as compared with α-MoB(111) and Mo_2B_4 (0001) surfaces. Therefore, NH_x intermediates hardly interact with $Mo_2B(001)$ surface which displays a low activity for eNRR (Fig. 4d). In contrast, NH* intermediate adsorbs strongest on Mo-terminated $Mo_2B_4(0001)$ surface resulting in a high limiting potential of − 0.41 V, also leading to a lower eNNR because of the highly endothermic reaction energy in ammonia synthesis by NH* hydrogenation (Fig. 4 f). The intermediate adsorption strength of NH_x on α-MoB endows α-MoB the highest activity for eNRR.

In consistence with the experimental literature that the molybdenum borides have a boron-dependent HER activity [40], our experimental results and DFT calculation show that Mo_2B_4 has the highest HER activity with the trend of Mo_2B_4 > α-MoB>Mo_2B (Figs. S11, S28). Together with the surface atomic structure (Fig. S18), we could conclude that more B occupancy at the surface/subsurface of molybdenum borides decreases hydrogen adsorption thus suppresses the HER activity. In other words, comparing to Mo_2B has too weak HER activity while Mo_2B_4 has too strong HER activity, α-MoB shows moderate HER. As is known, to achieve high FE, it requires high ammonia yield with a low rate of HER which is the case for α-MoB catalyst exhibiting the highest FE at the optimum yield potential (−0.15 V vs RHE) for eNRR. Our work paves an avenue to manipulate the FE of eNRR over molybdenum borides catalysts via surface HER activity by changing the boron occupancy at the surface/subsurface.

4. Conclusions

In summary, Mo_2B, α-MoB, and Mo_2B_4 powders were synthesized via a sintering process and used as catalysts in electrocatalytic ammonia production in this work. eNRR study showed that Mo_2B, α-MoB, and Mo_2B_4 demonstrated a peak NH_3 yield of 0.99 µg h^{-1} mg^{-1}, 5.45 µg h^{-1} mg^{-1}, 7.65 µg h^{-1} mg^{-1} at − 0.15 V vs RHE, respectively. Their FEs are 3.35 %, 17.17 %, and 12.47 %. The eNRR performance was qualitatively and quantitatively verified by isotope $^{15}N_2$ experiment. After normalized by electrochemically active surface area, α-MoB showed the highest intrinsic eNRR activity among the three molybdenum borides. DFT calculation revealed that α-MoB produces NH_3 via enzymatic and consecutive mechanisms with similar low energy barrier. Besides, the intermediate adsorption of NH_x and moderate HER activity contribute to the high eNRR activity of α-MoB with high selectivity. This work opens a window to explore molybdenum borides with low-valent Mo as efficient eNRR catalyst by taking advantage of their variable chemical compositions, crystal structures and tunable HER activities.

Author contributions

The manuscript was written through contributions of all authors. All authors have given approval to the final version of the manuscript.

Declaration of Competing Interest

The authors declare that they have no competing financial interests

or personal relationships that could have appeared to influence the work reported in this paper.

Data availability

Data will be made available on request.

Appendix A. Supporting information

Supplementary data associated with this article can be found in the online version at doi:10.1016/j.apcatb.2023.123020.

References

[1] G. Soloveichik, Electrochemical synthesis of ammonia as a potential alternative to the Haber–Bosch process, Nat. Catal. 2 (2019) 377–380.

[2] D.R. MacFarlane, P.V. Cherepanov, J. Choi, B.H.R. Suryanto, R.Y. Hodgetts, J. M. Bakker, F.M. Ferrero Vallana, A.N. Simonov, A roadmap to the ammonia economy, Joule 4 (2020) 1186–1205.

[3] C. Xia, Y. Xia, P. Zhu, L. Fan, H. Wang, Direct electrosynthesis of pure aqueous H_2O_2 solutions up to 20% by weight using a solid electrolyte, Science 366 (2019) 226–231.

[4] M.C. Leech, A.D. Garcia, A. Petti, A.P. Dobbs, K. Lam, Organic electrosynthesis: from academia to industry, React. Chem. Eng. 5 (2020) 977–990.

[5] D. Pollok, S.R. Waldvogel, Electro-organic synthesis - a 21st century technique, Chem. Sci. 11 (2020) 12386–12400.

[6] Z.J. Schiffer, K. Manthiram, Electrification and decarbonization of the chemical industry, Joule 1 (2017) 10–14.

[7] J.G. Chen, R.M. Crooks, L.C. Seefeldt, K.L. Bren, R.M. Bullock, M.Y. Darensbourg, P.L. Holland, B. Hoffman, M.J. Janik, A.K. Jones, M.G. Kanatzidis, P. King, K. M. Lancaster, S.V. Lymar, P. Pfromm, W.F. Schneider, R.R. Schrock, Beyond fossil fuel-driven nitrogen transformations, Science 360 (2018), eaar6611.

[8] S.L. Foster, S.I.P. Bakovic, R.D. Duda, S. Maheshwari, R.D. Milton, S.D. Minteer, M. J. Janik, J.N. Renner, L.F. Greenlee, Catalysts for nitrogen reduction to ammonia, Nat. Catal. 1 (2018) 490–500.

[9] B.H.R. Suryanto, H.-L. Du, D. Wang, J. Chen, A.N. Simonov, D.R. MacFarlane, Challenges and prospects in the catalysis of electroreduction of nitrogen to ammonia, Nat. Catal. 2 (2019) 290–296.

[10] W. Guo, K. Zhang, Z. Liang, R. Zou, Q. Xu, Electrochemical nitrogen fixation and utilization: theories, advanced catalyst materials and system design, Chem. Soc. Rev. 48 (2019) 5658–5716.

[11] Y.-C. Hao, Y. Guo, L.-W. Chen, M. Shu, X.-Y. Wang, T.-A. Bu, W.-Y. Gao, N. Zhang, X. Su, X. Feng, J.-W. Zhou, B. Wang, C.-W. Hu, A.-X. Yin, R. Si, Y.-W. Zhang, C.-H. Yan, Promoting nitrogen electroreduction to ammonia with bismuth nanocrystals and potassium cations in water, Nat. Catal. 2 (2019) 448–456.

[12] J. Zhao, Z. Chen, Single Mo atom supported on defective boron nitride monolayer as an efficient electrocatalyst for nitrogen fixation: a computational study, J. Am. Chem. Soc. 139 (2017) 12480–12487.

[13] M. Wang, S. Liu, T. Qian, J. Liu, J. Zhou, H. Ji, J. Xiong, J. Zhong, C. Yan, Over 56.55% Faradaic efficiency of ambient ammonia synthesis enabled by positively shifting the reaction potential, Nat. Commun. 10 (2019) 341.

[14] X. Liu, Y. Jiao, Y. Zheng, M. Jaroniec, S.Z. Qiao, Building up a picture of the electrocatalytic nitrogen reduction activity of transition metal single-atom catalysts, J. Am. Chem. Soc. 141 (2019) 9664–9672.

[15] X. Guo, J. Gu, S. Lin, S. Zhang, Z. Chen, S. Huang, Tackling the activity and selectivity challenges of electrocatalysts toward the nitrogen reduction reaction via atomically dispersed biatom catalysts, J. Am. Chem. Soc. 142 (2020) 5709–5721.

[16] Z. Fang, P. Wu, Y. Qian, G. Yu, Gel-derived amorphous bismuth-nickel alloy promotes electrocatalytic nitrogen fixation via optimizing nitrogen adsorption and activation, Angew. Chem. Int. Ed. 60 (2021) 4275–4281.

[17] C. Lv, C. Yan, G. Chen, Y. Ding, J. Sun, Y. Zhou, G. Yu, An amorphous noble-metal-free electrocatalyst that enables nitrogen fixation under ambient conditions, Angew. Chem. Int. Ed. 57 (2018) 6073–6076.

[18] C. Lv, L. Zhong, Y. Yao, D. Liu, Y. Kong, X. Jin, Z. Fang, W. Xu, C. Yan, K.N. Dinh, M. Shao, L. Song, G. Chen, S. Li, Q. Yan, G. Yu, Boosting electrocatalytic ammonia production through mimicking "π back-donation", Chem 6 (2020) 2690–2702.

[19] Y. Qian, Y. Liu, Y. Zhao, X. Zhang, G. Yu, Single vs double atom catalyst for N₂ activation in nitrogen reduction reaction: a DFT perspective, EcoMat 2 (2020), e12014.

[20] C. J. H.J acobsen, S. Dahl, B.S. Clausen, S. Bahn, A. Logadottir, J.K. Nørskov, Catalyst design by interpolation in the periodic table: bimetallic ammonia synthesis catalysts, J. Am. Chem. Soc. 123 (2001) 8404–8405.

[21] X. Guo, X. Wan, J. Shui, Molybdenum-based materials for electrocatalytic nitrogen reduction reaction, Cell Rep. Phys. Sci. 2 (2021), 100447.

[22] E. Skulason, T. Bligaard, S. Gudmundsdottir, F. Studt, J. Rossmeisl, F. Abild-Pedersen, T. Vegge, H. Jonsson, J.K. Norskov, A theoretical evaluation of possible transition metal electro-catalysts for N₂ reduction, Phys. Chem. Chem. Phys. 14 (2012) 1235–1245.

[23] H. Cheng, L.X. Ding, G.F. Chen, L. Zhang, J. Xue, H. Wang, Molybdenum carbide nanodots enable efficient electrocatalytic nitrogen fixation under ambient conditions, Adv. Mater. 30 (2018), e1803694.

[24] L. Zhang, X. Ji, X. Ren, Y. Ma, X. Shi, Z. Tian, A.M. Asiri, L. Chen, B. Tang, X. Sun, Electrochemical ammonia synthesis via nitrogen reduction reaction on a MoS₂ catalyst: theoretical and experimental studies, Adv. Mater. 30 (2018), e1800191.

[25] D. Yang, T. Chen, Z. Wang, Electrochemical reduction of aqueous nitrogen (N₂) at a low overpotential on (110)-oriented Mo nanofilm, J. Mater. Chem. A 5 (2017) 18967–18971.

[26] Y. Ohki, K. Munakata, Y. Matsuoka, R. Hara, M. Kachi, K. Uchida, M. Tada, R. E. Cramer, W.M.C. Sameera, T. Takayama, Y. Sakai, S. Kuriyama, Y. Nishibayashi, K. Tanifuji, Nitrogen reduction by the Fe sites of synthetic Mo₃S₄Fe cubes, Nature 607 (2022) 86–90.

[27] H. Tanaka, Y. Nishibayashi, K. Yoshizawa, Interplay between theory and experiment for ammonia synthesis catalyzed by transition metal complexes, Acc. Chem. Res. 49 (2016) 987–995.

[28] D.V. Yandulov, R.R. Schrock, Catalytic reduction of dinitrogen to ammonia at a single molybdenum center, Science 301 (2003) 76–78.

[29] C. Ling, X. Bai, Y. Ouyang, A. Du, J. Wang, Single molybdenum atom anchored on N-doped carbon as a promising electrocatalyst for nitrogen reduction into ammonia at ambient conditions, J. Phys. Chem. C 122 (2018) 16842–16847.

[30] Q. Zhao, Q. Cai, Y. Li, S. Wang, Y. Sun, Q. Zhou, D. Zhao, Single-atom Mo anchored on a poly(heptazine imide) nanosheet as a novel electrocatalyst showing excellent behavior toward nitrogen reduction reaction, J. Phys. Chem. C 126 (2022) 7859–7869.

[31] X.W. Lv, X.L. Liu, Y.J. Suo, Y.P. Liu, Z.Y. Yuan, Identifying the dominant role of pyridinic-N-Mo bonding in synergistic electrocatalysis for ambient nitrogen reduction, ACS Nano 15 (2021) 12109–12118.

[32] X. Li, T. Li, Y. Ma, Q. Wei, W. Qiu, H. Guo, X. Shi, P. Zhang, A.M. Asiri, L. Chen, B. Tang, X. Sun, Boosted electrocatalytic N₂ reduction to NH₃ by defect-rich MoS₂ nanoflower, Adv. Energy Mater. 8 (2018) 1801357.

[33] Y. Wan, Z. Wang, J. Li, R. Lv, Mo₂C-MoO₂ heterostructure quantum dots for enhanced electrocatalytic nitrogen reduction to ammonia, ACS Nano 16 (2022) 643–654.

[34] J. Wang, Z. Jiang, G. Peng, E. Hoenig, G. Yan, M. Wang, Y. Liu, X. Du, C. Liu, Surface valence state effect of MoO₂₊ₓ on electrochemical nitrogen reduction, Adv. Sci. 9 (2022), e2104857.

[35] X. Guo, X. Li, Y. Li, J. Yang, X. Wan, L. Chen, J. Liu, X. Liu, R. Yu, L. Zheng, J. Shui, Molecule template method for precise synthesis of Mo-based alloy clusters and electrocatalytic nitrogen reduction on partially reduced PtMo alloy oxide cluster, Nano Energy 78 (2020), 105211.

[36] X. Guo, X. Wan, Q. Liu, Y. Li, W. Li, J. Shui, Phosphated IrMo bimetallic cluster for efficient hydrogen evolution reaction, eScience 2 (2022) 304–310.

[37] X. Liu, Y. Jiao, Y. Zheng, S.-Z. Qiao, Isolated boron sites for electroreduction of dinitrogen to ammonia, ACS Catal. 10 (2020) 1847–1854.

[38] H.Y. Zhou, Y.B. Qu, J.C. Li, Z.L. Wang, C.C. Yang, Q. Jiang, Effectively boosting selective ammonia synthesis on electron-deficient surface of MoB₂, Appl. Catal. B Environ. 305 (2022), 121023.

[39] Y. Fu, P. Richardson, K. Li, H. Yu, B. Yu, S. Donne, E. Kisi, T. Ma, Transition metal aluminum boride as a new candidate for ambient-condition electrochemical ammonia synthesis, Nano Micro Lett. 12 (2020) 65.

[40] H. Park, A. Encinas, J.P. Scheifers, Y. Zhang, B.P.T. Fokwa, Boron-dependency of molybdenum boride electrocatalysts for the hydrogen evolution reaction, Angew. Chem. Int. Ed. 56 (2017) 5575–5578.

[41] A.H. Dismukes, Binary and Ternary Explorations of the Molybdenum Boride System (Master thesis), University of California, Los Angeles (US), (2015).

[42] X. Wang, G. Tai, Z. Wu, T. Hu, R. Wang, Ultrathin molybdenum boride films for highly efficient catalysis of the hydrogen evolution reaction, J. Mater. Chem. A 5 (2017) 23471–23475.

[43] Y. Chen, G. Yu, W. Chen, Y. Liu, G.D. Li, P. Zhu, Q. Tao, Q. Li, J. Liu, X. Shen, H. Li, X. Huang, D. Wang, T. Asefa, X. Zou, Highly active, nonprecious electrocatalyst comprising borophene subunits for the hydrogen evolution reaction, J. Am. Chem. Soc. 139 (2017) 12370–12373.

[44] H. Tang, X. Gao, J. Zhang, B. Gao, W. Zhou, B. Yan, X. Li, Q. Zhang, S. Peng, D. Huang, L. Zhang, X. Yuan, B. Wan, C. Peng, L. Wu, D. Zhang, H. Liu, L. Gu, F. Gao, T. Irifune, R. Ahuja, H.-K. Mao, H. Gou, Boron-rich molybdenum boride with unusual short-range vacancy ordering, anisotropic hardness, and superconductivity, Chem. Mater. 32 (2019) 459–467.

[45] H. Chen, X. Zou, Intermetallic borides: structures, synthesis and applications in electrocatalysis, Inorg. Chem. Front. 7 (2020) 2248–2264.

[46] H. Vrubel, X. Hu, Molybdenum boride and carbide catalyze hydrogen evolution in both acidic and basic solutions, Angew. Chem. Int. Ed. 51 (2012) 12703–12706.

[47] H. Park, Y. Zhang, J.P. Scheifers, P.R. Jothi, A. Encinas, B.P.T. Fokwa, Graphene- and phosphorene-like boron layers with contrasting activities in highly active Mo₂B₄ for hydrogen evolution, J. Am. Chem. Soc. 139 (2017) 12915–12918.

[48] G. Peng, J. Wu, M. Wang, J. Niklas, H. Zhou, C. Liu, Nitrogen-defective polymeric carbon nitride nanolayer enabled efficient electrocatalytic nitrogen reduction with high faradaic efficiency, Nano Lett. 20 (2020) 2879–2885.

[49] W. Kohn, Nobel lecture: electronic structure of matter—Wave functions and density functionals, Rev. Mod. Phys. 71 (1999) 1253–1266.

[50] J.A. Steckel, Density Functional theory: a Practical Introduction, Wiley-VCH, Weinheim, 2011.

[51] Y. Li, L. Li, R. Huang, Y. Wen, Computational screening of MBene monolayers with high electrocatalytic activity for the nitrogen reduction reaction, Nanoscale 13 (2021) 15002–15009.

[52] M. Che, Nobel prize in chemistry 1912 to Sabatier: organic chemistry or catalysis? Catal. Today 218–219 (2013) 162–171.